Physics of Plasmas ARTICLE scitation.org/journal/php

# GTC simulation of linear stability of tearing mode and a model magnetic island stabilization by ECCD in toroidal plasma

Cite as: Phys. Plasmas **27**, 042507 (2020); doi: 10.1063/1.5111127
Submitted: 23 May 2019 · Accepted: 16 March 2020 ·
Published Online: 2 April 2020



Jingchun Li,[1,2,3,a)] Chijie Xiao,[1] Zhihong Lin,[3] Dongjian Liu,[4] Xiaoquan Ji,[5] and Xiaogang Wang[6]

## AFFILIATIONS

[1]Fusion Simulation Center, Peking University, Beijing 100871, People's Republic of China
[2]School of Physics, Nankai University, Tianjin 300071, People's Republic of China
[3]University of California, Irvine, California 92697, USA
[4]Sichuan University, Chengdu 610064, People's Republic of China
[5]Southwestern Institute of Physics, Chengdu 610041, People's Republic of China
[6]Harbin Institute of Technology, Harbin 150001, People's Republic of China

[a)]Author to whom correspondence should be addressed: jingchunli@pku.edu.cn

## ABSTRACT

Stabilization of a model magnetic island in tokamaks by localized electron cyclotron current drive (ECCD) has been studied using a fluid-kinetic hybrid model coupled with ray tracing and Fokker–Planck equations. Even though a gyrokinetic toroidal code at present is not able to simulate the long-time evolution of tearing modes, which starts from small perturbation and evolves to the Rutherford regime, we can still calculate a model magnetic island and its stabilization by ECCD. Gyrokinetic simulations find that the model magnetic island can be fully stabilized by the ECCD with the 1 MW 68 GHz X2-mode in HL-2A-like equilibrium, while the model magnetic island in the DIII-D tokamak is only partially stabilized with the same ECCD power. A helicoidal current drive is more efficient than a continuous ECCD to stabilize the model magnetic island. Simulation results further indicate that, without external current drive, thermal ion kinetic effects could also reduce the magnetic island width and the linear growth rate of tearing modes.



## I. INTRODUCTION

Tearing mode (TM) instabilities can degrade plasma performance and may even lead to disruptions.[1–4] Various methods for TM control have been established and verified in experiments such as electron cyclotron current drive (ECCD),[5,6] lower hybrid current drive,[7] externally applied resonant magnetic perturbations,[8,9] and neutral beam injection.[10] Since ECCD can be highly localized and robustly controlled, it is considered to be an effective and successful method of controlling TMs. Experiments of ECCD and electron cyclotron resonant heating (ECRH) on many devices such as ASDEX Upgrade,[11] DIII-D,[12] and JT-60U[13] have shown complete suppression of TMs or neoclassical tearing modes (NTMs),[14] a class of tearing modes driven by bootstrap current. Moreover, results in DIII-D have also shown that the stationary operation of hybrid scenario plasmas was successfully attained until the ECCD was turned off, suggesting that tearing mode stabilization with ECCD is critical for stable operation.[15]

The TM stabilization conditions have been achieved in the HL-2A tokamak,[16,17] so this device is considered here as a typical case for the tearing mode suppression. Only TM stabilization by ECRH has been achieved in HL-2A experiments. Similar experiments have also been reported in TCV,[18] TEXTOR,[19] ASDEX Upgrade,[20] etc. TM stabilization by ECCD requires a toroidal component to the electron cyclotron (EC) injection. In DIII-D, La Haye *et al.* used active feedback to control the neoclassical tearing mode.[21] Subsequently, the complete suppression of the $m/n = 2/1$ neoclassical tearing mode was achieved using ECCD to replace the missing bootstrap current in the island's O-point.[22]

Since the TMs and neoclassical tearing mode stabilization by ECCD are still under investigation, it is essential to conduct the corresponding simulations in order to facilitate and test the design of the real-time control system for TMs. Numerical studies of TM stabilization by ECCD have been carried out using various numerical algorithms.[23–28] Some of these algorithms are based on the full MHD in

toroidal geometries. Popov *et al.* have simulated the TM suppression by a radially localized toroidal current from ECCD[29] with a full MHD code. Jenkins has calculated the TM stabilization with ECCD using the NIMROD code and demonstrated the complete suppression of the (2,1) tearing mode.[30] However, these works fall short of realizing a fully coupled, self-consistent model for ECCD/MHD interaction, including toroidal effects and kinetic effects.

In fusion plasmas, the ions can have significant kinetic effects on the evolution of tearing modes. Analytically, Cai *et al.* found that the co-circulating energetic ions can stabilize the TMs.[31] Subsequently, they reported the effects of energetic particles on TMs from M3D-K simulations.[32] In their model, background thermal ions and electrons are treated as a single fluid, and the energetic ions are described by the drift kinetic equation. Hornsby *et al.* studied the nonlinear tearing mode evolution with the gyro-kinetic code GKW and their self-consistent interaction with electromagnetic turbulence.[33] The kinetic effects of thermal ions on the TM stabilization are an important area of study that has not been investigated thoroughly.

We have performed kinetic simulations of tearing modes and their suppression with localized current drive in tokamak plasmas by using the gyrokinetic toroidal code (GTC),[34] which has been extensively applied to study neoclassical transport,[35] energetic particle transport,[36] Alfvén eigenmodes,[37,38] microturbulence,[39] and current-driven instabilities including kink[40] and tearing modes.[41,42] In Ref. 42, we studied the effect of ECCD on the magnetic island. However, the ECCD model used there is an analytical model, and simulations were performed in a cylinder.

In order to study the influence of ECCD on TMs more precisely and guide the future experiments of TM stabilization on specific tokamaks, we carry out gyrokinetic simulations[43] in toroidal geometry. The effect of ECCD on a model magnetic island is investigated through the coupling between the GTC and GENRAY/CQL3D package[44] with ECCD ray tracing and Fokker-Planck operators. The current GTC simulations find that the TM magnetic island can be perfectly stabilized by the 1 MW 68 GHz X2-mode in the HL-2A tokamak, while instabilities in the DIII-D discharge are only partially stabilized with the 1 MW 110 GHz X2-mode ECCD due to inadequate power input. Our simulation finds that a helicoidal current drive is more efficient than a continuous ECCD. This means that ECCD current deposition at the O point is more efficient than continuous deposition, and our results are consistent with previous simulation results.[24,45] These simulation results also indicate, both in HL-2A and DIII-D, that the presence of thermal ion kinetic effects can reduce the island width and the linear growth rate, and the kinetic effect of thermal ions on TMs is more pronounced with higher ion temperature.

The remainder of this paper is organized as follows: The simulation model of TM suppression by ECCD is introduced in Sec. II. The driven current characteristics and its mechanism for controlling the model magnetic island, as well as the ion kinetic effects on the TM stabilization, are presented in Sec. III. Finally, brief conclusions are drawn in Sec. IV.

## II. MODELING

In order to study the low-frequency MHD instabilities, such as resistive tearing modes, a massless electron fluid model can be coupled with gyrokinetic ions through the gyrokinetic Poisson's equation and Ampère's law.[41] In this work, we neglect the electron kinetic effects, which has been implemented in GTC using a fluid-kinetic hybrid electron model[46] and a conservative scheme for solving the electron drift kinetic equation.[47] To study the effects of ECCD on TM, the ECCD current is obtained by employing the GENRAY/CQL3D code, which solves ray-tracing and Fokker-Planck equations.

### A. Gyrokinetic ion and massless electron fluid model

The gyrokinetic equation[48,49] describing toroidal (magnetized) plasmas in the inhomogeneous magnetic field is given by

$$\frac{\mathrm{d}}{\mathrm{d}t}f_\alpha(\boldsymbol{X},\mu,v_\parallel,t)=\left(\frac{\partial}{\partial t}+\dot{\boldsymbol{X}}\cdot\nabla+\dot{v}_\parallel\frac{\partial}{\partial v_\parallel}\right)f_\alpha=\left(\frac{\partial}{\partial t}f_\alpha\right)_{collsion}, \quad (1)$$

$$\dot{\boldsymbol{X}}=v_\parallel\frac{\boldsymbol{B}}{B_0}+\frac{c\boldsymbol{b_0}\times\nabla\phi}{B_0}+\frac{v_\parallel^2}{\Omega_\alpha}\nabla\times\boldsymbol{b_0}+\frac{\mu}{m_\alpha\Omega_\alpha}\boldsymbol{b_0}\times\nabla B_0, \quad (2)$$

$$\dot{v}_\parallel=-\frac{1}{m_\alpha}\frac{\boldsymbol{B}^*}{B_\parallel^*}\cdot(\mu\nabla B_0+Z_i\nabla\phi)-\frac{Z_\alpha}{m_\alpha c}\frac{\partial A_\parallel}{\partial t}. \quad (3)$$

Here, index $\alpha=e,i$ stands for the particle species, electron or ion. $\boldsymbol{X}$, $\mu$, are $v_\parallel$ are the particle guiding center position, the magnetic moment, and the parallel velocity. $\phi$, $A_\parallel$ are the electrostatic potential and parallel vector potential, respectively, and both are gyro-averaging for ions. $Z_\alpha$ is the particle charge, $m_\alpha$ and $\Omega_\alpha$ are the particle mass and cyclotron frequency, $\boldsymbol{B_0}\equiv B_0\boldsymbol{b_0}$ is the equilibrium magnetic field, $\boldsymbol{B_0^*}=\boldsymbol{B_0}+(B_0v_\parallel/\Omega_\alpha)\nabla\times\boldsymbol{b_0}$, $B_\parallel^*=\boldsymbol{b_0}\cdot\boldsymbol{B_0^*}$, and the expression of $\boldsymbol{B}^*$ can be found in Ref. 47. $\boldsymbol{B}\equiv\boldsymbol{B_0}+\delta\boldsymbol{B}$, which incorporates all the magnetic perturbation. For the electron, a Krook collisional operator, $\frac{\partial}{\partial t}f_{e0}=\eta(f_e-f_{e0})$, is used to provide resistivity, where $f_{e0}$ is the equilibrium distribution function. For the ion, the collision operator $\left(\frac{\partial}{\partial t}f_i\right)_{collsion}$ has been implemented in GTC; however, as in Ref. 42, we will omit it in this work.

To reduce particle noises, a perturbative ($\delta f$) simulation scheme has been used.[50,51] Assuming a neoclassical solution for the equilibrium distribution function ($f_{\alpha0}$) that satisfies the equilibrium drift kinetic equation

$$L_0f_{\alpha0}=0, \quad (4)$$

where $L_0=\frac{\partial}{\partial t}+(v_\parallel\boldsymbol{b_0}+\boldsymbol{v}_d)\cdot\nabla-\frac{\mu}{m_\alpha}\boldsymbol{b_0}\frac{\partial}{\partial v_\parallel}$ is the equilibrium propagator. Subtracting Eq. (1) by Eq. (4), the equation for the perturbed distribution $\delta f_\alpha$ is

$$L\delta f_\alpha=-\delta Lf_{\alpha0}, \quad (5)$$

where $\delta L=\left(v_\parallel\frac{\boldsymbol{\delta B}}{B_0}+\boldsymbol{v}_E\right)\cdot\nabla-\left(\frac{\mu}{m_\alpha}\frac{\boldsymbol{\delta B}}{B_0}\cdot\nabla B_0+\frac{q_\alpha}{m_\alpha}E_\parallel-\frac{q_\alpha}{m_\alpha}\frac{\boldsymbol{v}_\epsilon}{v_\parallel}\cdot\nabla\phi\right)\frac{\partial}{\partial v_\parallel}$, $L=L_0+\delta L$. On the right side of Eq. (5), we use a shift Maxwellian as an approximation of the neoclassical solution ($f_0$). Defining the particle weight as $w_\alpha=\delta f_\alpha/f_\alpha$, we can rewrite Eq. (1) as the weight equation by using Eq. (5)

$$\frac{dw_\alpha}{dt}=(1-w_\alpha)\left[-\left(v_\parallel\frac{\delta\boldsymbol{B}}{B_0}+\boldsymbol{v}_E\right)\cdot\frac{\nabla f_{\alpha0}}{f_{\alpha0}}+\left(\mu\frac{\delta\boldsymbol{B}}{B_0}\cdot\nabla B_0+q_\alpha\frac{\boldsymbol{B}^*}{B_0}\cdot\nabla\phi+\frac{q_\alpha}{c}\frac{\partial A_\parallel}{\partial t}\right)\frac{1}{m_\alpha}\frac{1}{f_{\alpha0}}\frac{\partial f_{\alpha0}}{\partial v_\parallel}\right]. \quad (6)$$

The dynamic equation [Eq. (6)] together with the field equations [see Eqs. (11) and (12)] forms the closed system of equations for the

nonlinear gyrokinetic simulations. For ions, we use these standard gyrokinetic formulations. For electrons, we integrate Eq. (1) to get the perturbed fluid continuity equation

$$\begin{aligned}&\frac{\partial}{\partial t}\delta n_e+\boldsymbol{B_0}\cdot\nabla\left(\frac{n_{e0}\delta u_{\parallel e}}{B_0}\right)+B_0\delta\boldsymbol{v_E}\cdot\nabla\left(\frac{n_e}{B_0}\right)\\&-n_{e0}(\delta\boldsymbol{v}_{*\boldsymbol{e}}+\delta\boldsymbol{v_E})\cdot\frac{\nabla B_0}{B_0}+\delta\boldsymbol{B}\cdot\nabla\left(\frac{n_{e0}\delta u_{\parallel e0}}{B_0}\right)\\&+\frac{c\nabla\times\boldsymbol{B_0}}{B_0^2}\cdot\left(-\frac{\nabla\delta p_e}{e}+n_{e0}\nabla\delta\phi\right)\\&+\left\{\delta\boldsymbol{B}\cdot\nabla\left(\frac{n_{e0}\delta u_{\parallel e}}{B_0}\right)+B_0\delta\boldsymbol{v_E}\cdot\nabla\left(\frac{\delta n_e}{B_0}\right)\right.\\&\left.+\frac{c\nabla\times\boldsymbol{B_0}}{B_0^2}\cdot\delta n_e\nabla\delta\phi\right\}_{NL}=0\end{aligned}\tag{7}$$

and the parallel momentum equation

$$\begin{aligned}&n_{e0}m_e\frac{\partial}{\partial t}\delta u_{\parallel e}+n_{e0}m_e\boldsymbol{u}_{\parallel e0}\cdot\nabla\delta u_{\parallel e}\\&=-n_{e0}e\left(-\nabla_\parallel\delta\phi-\frac{1}{c}\frac{\partial\delta A_\parallel}{\partial t}\right)-\frac{\delta\boldsymbol{B}}{B_0}\cdot\nabla p_{e0}\\&-\nabla_\parallel\delta p_e-n_{e0}m_e\nu_{ei}\delta u_{\parallel e},\end{aligned}$$

with the total electron density $n_e$, parallel flow $u_{\parallel e}$, and pressure $p_e$ the sum of their equilibrium and perturbed parts, i.e., $n_e=n_{e0}+\delta n_e$, $u_{\parallel e}=u_{\parallel e0}+\delta u_{\parallel e}$, and $p_e=p_{e0}+\delta p_e$. Since this work is focused on the resistive tearing mode, we neglect the electron inertial term on the left hand side of the momentum equation. Furthermore, we treat the effect of the ECCD source entering as an additional force on the electron fluid, thereby reducing the massless electron momentum equation to the parallel force balance equation

$$\frac{\partial\delta A_\parallel}{\partial t}=-c\boldsymbol{b_0}\cdot\nabla\delta\phi+\frac{c}{n_{e0}e}\boldsymbol{b_0}\cdot\nabla\delta p_e-c\eta(\delta j-\delta j_{eccd}-\delta j_{bs}).\tag{8}$$

Here, $\delta j=-\frac{c}{4\pi}\nabla_\perp^2\delta A_\parallel$, $\delta j_{eccd}$ is the EC-driven current density, And $\delta j_{bs}$ is the perturbed bootstrap current, which has a simple form

$$\delta j_{bs}=-1.46\frac{\sqrt{(\varepsilon_0)}}{B_\theta}\frac{\partial\delta p}{\partial r}.\tag{9}$$

We need an additional pressure diffusion equation to cover the pressure flatting effect inside the magnetic island

$$\begin{aligned}\frac{d\delta p}{dr}&=\chi_\parallel\hat{\nabla}_\parallel^2\delta p+\chi_\perp\nabla_\perp^2\delta p\\&=\chi_\parallel\nabla_\parallel^2\delta p+\chi_\parallel\nabla_\parallel\left(\frac{\delta\boldsymbol{B}}{B_0}\cdot\nabla P\right)+\chi_\perp\nabla_\perp^2\delta p\\&+\chi_\parallel\left[\frac{\delta\boldsymbol{B}}{B_0}\cdot\nabla\left(\nabla_\parallel\delta p+\frac{\delta\boldsymbol{B}}{B_0}\cdot\nabla\delta p+\frac{\delta\boldsymbol{B}}{B_0}\cdot\nabla p_0\right)\right.\\&\left.+\nabla_\parallel\left(\frac{\delta\boldsymbol{B}}{B_0}\cdot\delta p\right)\right]_{NL},\end{aligned}\tag{10}$$

where $\hat{\nabla}_\parallel^2$ is the gradient operator defined along the total magnetic field and $\nabla_\parallel$ and $\nabla_\perp$ are the operators defined along the equilibrium magnetic field. With Eqs. (9) and (10), we could study the bootstrap current effect; however, since this article focuses on TMs, the calculations in this paper do not consider the $\delta j_{bs}$ term except for special statements. In order to complete the fluid model, we use the gyrokinetic Poisson's equation

$$\frac{4\pi Z_i^2}{T_i}(\delta\phi-\delta\tilde{\phi})=4\pi(Z_i\delta n_i-e\delta n_e)\tag{11}$$

and the parallel Ampère's law

$$en_{e0}\delta u_{\parallel e}=\delta j+Z_in_{i0}\delta u_{\parallel i},\tag{12}$$

where $n_i$ and $u_{\parallel i}$ can be calculated from the standard gyrokinetic model for ions,[46] namely, Eqs. (1)–(6).

The gyrokinetic ions (1)–(6) and fluid electrons (7) and (8) are coupled through Eqs. (11) and (12). These equations form a closed system, which can simulate the low frequency MHD instabilities. It should be noted that for the fluid simulations, we treat both electrons and ions as fluid. The reduction of the ion gyrokinetic equation to ideal MHD equations has been shown in Ref. 52, which is neglected here. The difference between the electron and ion continuity equation is that the introduction of the term of the ion finite Larmor radius effect.

### B. Model for electron cyclotron current drive

The ECCD current is calculated using the GENRAY/CQL3D software package.[44] The two principal equations solved in the package are ray-tracing equations and Fokker–Planck equation.

The ray-tracing equations are

$$\frac{\mathrm{d}R}{\mathrm{d}t}=-\frac{c}{\omega}\frac{\partial D_0/\partial N_R}{\partial D_0/\partial\omega};\quad\frac{\mathrm{d}N_R}{\mathrm{d}t}=\frac{c}{\omega}\frac{\partial D_0/\partial R}{\partial D_0/\partial\omega},\tag{13}$$

$$\frac{\mathrm{d}\varphi}{\mathrm{d}t}=-\frac{c}{\omega}\frac{\partial D_0/\partial M}{\partial D_0/\partial\omega};\quad\frac{\mathrm{d}M}{\mathrm{d}t}=\frac{c}{\omega}\frac{\partial D_0/\partial\varphi}{\partial D_0/\partial\omega},\tag{14}$$

$$\frac{\mathrm{d}Z}{\mathrm{d}t}=-\frac{c}{\omega}\frac{\partial D_0/\partial N_Z}{\partial D_0/\partial\omega};\quad\frac{\mathrm{d}N_Z}{\mathrm{d}t}=\frac{c}{\omega}\frac{\partial D_0/\partial Z}{\partial D_0/\partial\omega}.\tag{15}$$

Here, we use cylindrical coordinates $R=(R,\varphi,Z)$, where R is the major radius, $\varphi$ is the toroidal angle, and Z is along the vertical axis. $N=Kc/\omega=(N_R,M=RN_\varphi,N_Z)$. $D_0$ is the dispersion function calculated using the magnetized cold plasma approximation and is given in Ref. 44. In our calculations, the poloidal injection angle, $\alpha$, is defined with respect to the Z = constant plane at the source, with positive angles above the plane and negative below. The toroidal injection angle, $\beta$, is measured counterclockwise with respect to the Z axis. $\omega$ denotes the wave frequency, and the dispersion relation is calculated with cold plasma approximation.

The 3-dimensional bounce averaged Fokker–Planck equation, 2-D in momentum space (slowing down, pitch-angle), and 1-D in configuration space (radial dimension) for the electron distribution function $f_e$ are given by

$$\frac{\partial f_e}{\partial t}=\frac{\partial f_e}{\partial\boldsymbol{u}}D_{EC}\frac{\partial f_e}{\partial\boldsymbol{u}}+\hat{C}f_e,\tag{16}$$

where $D_{EC}$ is the diffusion coefficient of the electron cyclotron wave (ECW) in the velocity space, $\boldsymbol{u}=\boldsymbol{p}/m_e$ is the normalized momentum, and $\hat{C}$ is the collision operator. Solving the Fokker–Planck equation,

we obtain the distribution function. The driven current density can be calculated from

$$\delta j_{eccd}(\rho) = -en_{e0}c\int \frac{u_{\parallel}}{\gamma} f_e(\rho, \boldsymbol{u})\mathrm{d}\boldsymbol{u}. \quad (17)$$

Here, $\gamma$ is the electron relativistic factor and the radial variable $\rho = \sqrt{\psi/\psi_w}$ is defined as the square root of the normalized poloidal magnetic flux. Once the ECCD current is obtained from GENRAY/CQL3D, the effect of the ECCD on tearing modes can be implemented in the GTC through Eq. (8). If we use Eq. (17) as $\delta j_{eccd}$ in Eq. (8) directly, it means that we consider the continuous current drive by neglecting effects of magnetic islands. It is well known that the driven current at the O-point can suppress the tearing mode, while at the X-point, it leads to the destabilization of the tearing mode.[53,54] In the experiment, such a helical current has been generated by modulating continuous current drive, and better efficiency for suppressing tearing modes has been obtained.[54] Therefore, a helical driven current is also used to study the suppression of tearing modes. This kind of driven current density can be written as follows:

$$\delta j_{eccd} = \delta j_{eccd}(\rho)(1 + \cos(m\theta - n\xi)). \quad (18)$$

We do not consider the diffusion of fast electrons, that is, we do not consider the change in the current distribution in the direction of magnetic lines of force; however, our recent calculations show that the effect of the relaxation of fast electrons on the current does not play a dominate role, so we ignore this effect here, that is, we are not considering Eq. (5) in Ref. 24. It should be noted that due to timescale separations, the ray tracing and Fokker-Planck equation are not solved simultaneously with the hybrid model equation in the GTC. Thus, the effect of the magnetic perturbations on the wave deposition and the source current profile is neglected. Finally, compared with the model in Ref. 42, the ECCD model used here is more realistic because this current drive is calculated by solving ray-tracing equations and Fokker-Planck equations in the GENRAY/CQL3D package. However, in the former paper, the current term only applies an analytical formula without involving the RF-induced current.

## III. NUMERICAL ANALYSIS

We will demonstrate the feasibility of using our model to calculate the TM stabilization both with a HL-2A-like and a DIII-D equilibrium.

### A. Linear analysis of tearing modes in HL-2A-like equilibrium

An HL-2A model equilibrium is chosen in our simulation, i.e., the major radius is $R_0 = 1.65$ m, the minor radius is $a = 0.4$ m, and the on-axis magnetic field is $B_0 = 1.27$T. The equilibrium $q$ profile, electron density, and temperature profile utilized are shown in Fig. 1. The electron density and temperature profile are from experimental data,[55] while the $q$ profile is modified from EFIT-reconstruction since the initial $q$ distribution (the green line $q$ in Fig. 1) cannot get the growing TM, and the circular-cross section is assumed. Our calculation shows that it is the stronger magnetic shear that excites to the tearing mode in HL-2A. In the simulations, we use the number of grids $150 \times 350 \times 16$ in the radial, poloidal, and parallel directions, respectively. The equilibrium plasma current is 157 kA, the $q = 2/1$ surface is $r = 0.6a$, and the plasma resistivity is $\eta = 10^{-5}\,\Omega/\mathrm{m}$. The resistivity is higher than the Spitzer resistivity ($\eta \sim 10^{-8}\,\Omega/\mathrm{m}$ with the HL-2A parameter). This is because large time steps cause numerical errors in the finite difference model when the resistivity is very low. We have calculated the dependence of the linear growth rate on the resistivity and found that the dependence is similar to the theoretical resistivity scaling of tearing modes, i.e., $\eta^{3/5}$. The dependence of ECCD stabilization on $\eta$ is under investigation and not clarified in this paper.

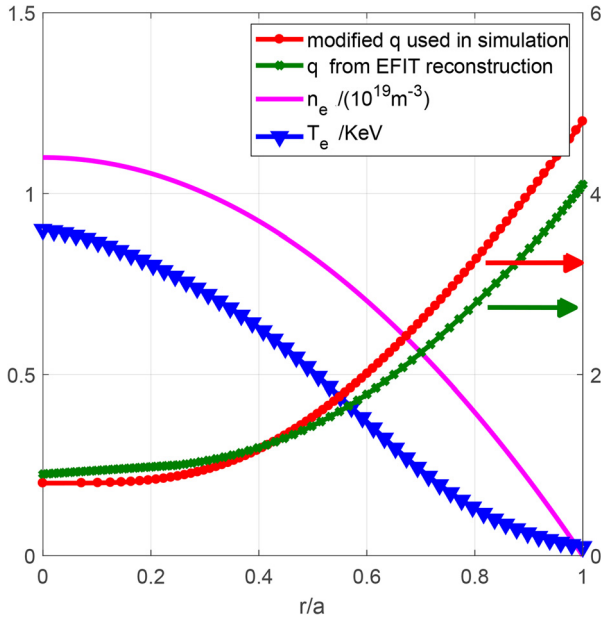


**FIG. 1.** Radial profiles of the safety factor $q$, electron density $n_e$, and temperature $T_e$ in HL-2A-like equilibrium.

We have verified the GTC capability of the resistive tearing mode simulation in Ref. 42; therefore, we utilize this capability for the tearing mode simulation in the above HL-2A configuration. It is found that the mode amplitude starts to increase at about $t = 1.7 \times 10^{-5}$ s. The corresponding magnetic island width is about $0.169a$ at this time, and the growth rate is $0.13\omega_s$, where the normalized frequency is $\omega_s \equiv c_s/R_0, c_s \equiv \sqrt{T_e/m_i}$ and $T_e$ is calculated at the $q = 2$ rational surface. Note that the initial magnetic island width (0.13a; when t = 0, the width of the magnetic island is measured by the contour map of the magnetic field lines) given here is dependent on the initial parallel vector perturbation potential, which is given by $A(r) = -0.658 \times 10^{-3}(r/a)^2(1 - r/a)^2$.

A typical electron cyclotron current drive in HL-2A-like equilibrium is shown in Fig. 2 for both continuous ECCD and helicoidal ECCD. Figure 2(a) shows the EC-wave trajectories on a poloidal plane, and Fig. 2(b) shows the current density vs major radius from the GENRAY/CQL3D calculations. In this case, the poloidal and toroidal injection angles are $\alpha = 113°$ and $\beta = 190°$, respectively, the wave power is 1 MW, and the wave frequency is the 68 GHz X2-mode. The total driven current here is 13 kA. The current ratio $CR \equiv I_{ECCD}/I_0 = 0.08$, and the corresponding current ratio at the mode rational surface between the current density by external current drive and the

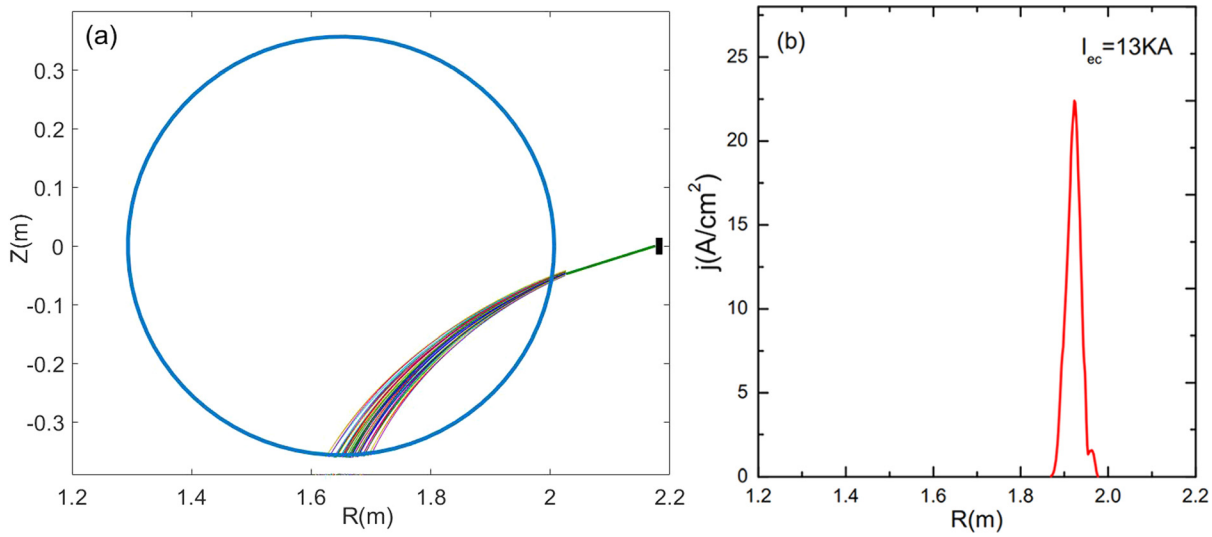


**FIG. 2.** (a) Electron cyclotron wave trajectories on a poloidal plane with the last closed field surface (LCFS) and (b) ECCD current density vs major radius.

perturbed current density is $\delta j_{eccd}/\delta j = 1.6$, with the radial deposition position located at $r/a = 0.6$, which is approximately at the rational surface of $q = 2$. The poloidal profiles of the TM perturbed current density and the helicoidal ECCD current density are shown in Fig. 3.

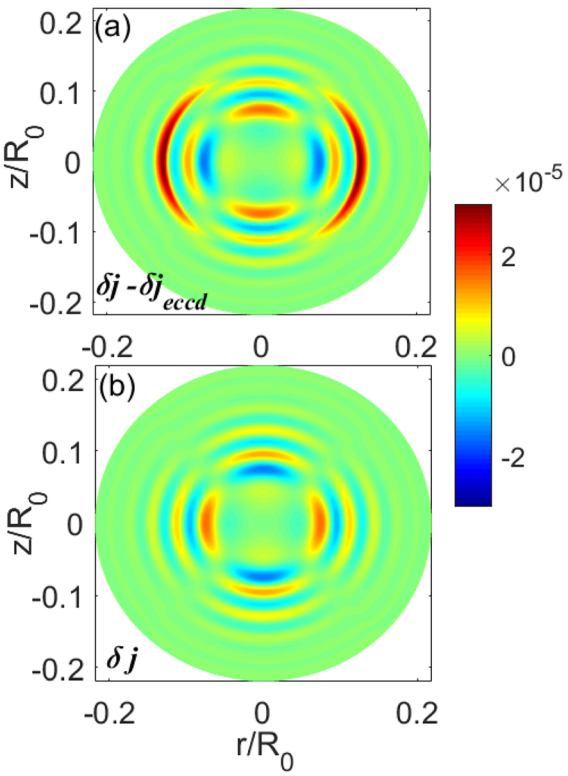


**FIG. 3.** The poloidal structure of TM perturbed current density (a) and helicoidal ECCD current density (b).

We find that without ECCD, the (2,1) TM amplitude increases. In the case of ECW injection, the width of the TM island decreases quickly and reduces to zero, and the growth rate of TMs becomes negative (decay rate of $0.10\omega_s$, where the decay rate is the slope of the mode amplitude that grows or decays in time), and thus, the TM is indeed stabilized by ECCD. It is also found that the helicoidal current drive is more efficient than the continuous ECCD. In comparison with continuous ECCD, the decay rate with helicoidal current drive is about $0.25\omega_s$. Previous studies by Wang *et al.*[26] showed that ECCD has a suppression effect on TMs when CR = 0 - 0.07, and ECCD has the best suppression efficiency at CR = 0.04. Our study in 2017[42] also showed that when CR = 0.04, ECCD can suppress the TM. However, these studies are limited to the continuous ECCD. In this work, we calculate and compare both the continuous and modulated ECCD cases. The modulated ECCD is 2.5 times better than the continuous ECCD in terms of stabilization, which provides a reference for future fusion experiments.

In general, the tearing mode in HL-2A is straightforward to suppress for this equilibrium parameter. Since the steering mirrors in the launcher allow the poloidal injection angle and the toroidal injection angle to be rotated between $-20°$ and $20°$, it is possible to inject the ECW off-axis, i.e., $r/a = 0.6$ in this case. The TM stabilization is closely related to the value of the current ratio CR ($CR \equiv I_{rf}/I_0$). Our study found that the tearing mode can be completely suppressed when the current ratio CR is about 0.08. The equilibrium plasma current $I_0$ is low in this case. However, the total ECW power of 3 MW (Ref. 56) is sufficient to suppress the TMs, even if $I_0$ reaches the highest value in HL-2A (450 kA). Finally, the dependence of the TM magnetic island width and growth rates on wave radial misalignment has been investigated in Ref. 42.

We study the kinetic effects of thermal ions in the GTC simulations. In our simulation, the number of grids $150 \times 350 \times 16$ in the radial, poloidal, and parallel directions are used. We adopt the same HL-2A parameters as in Sec. III A and load 20 ions in every cell. Figure 4 shows the mode structure [(a) and (b)] and the magnetic

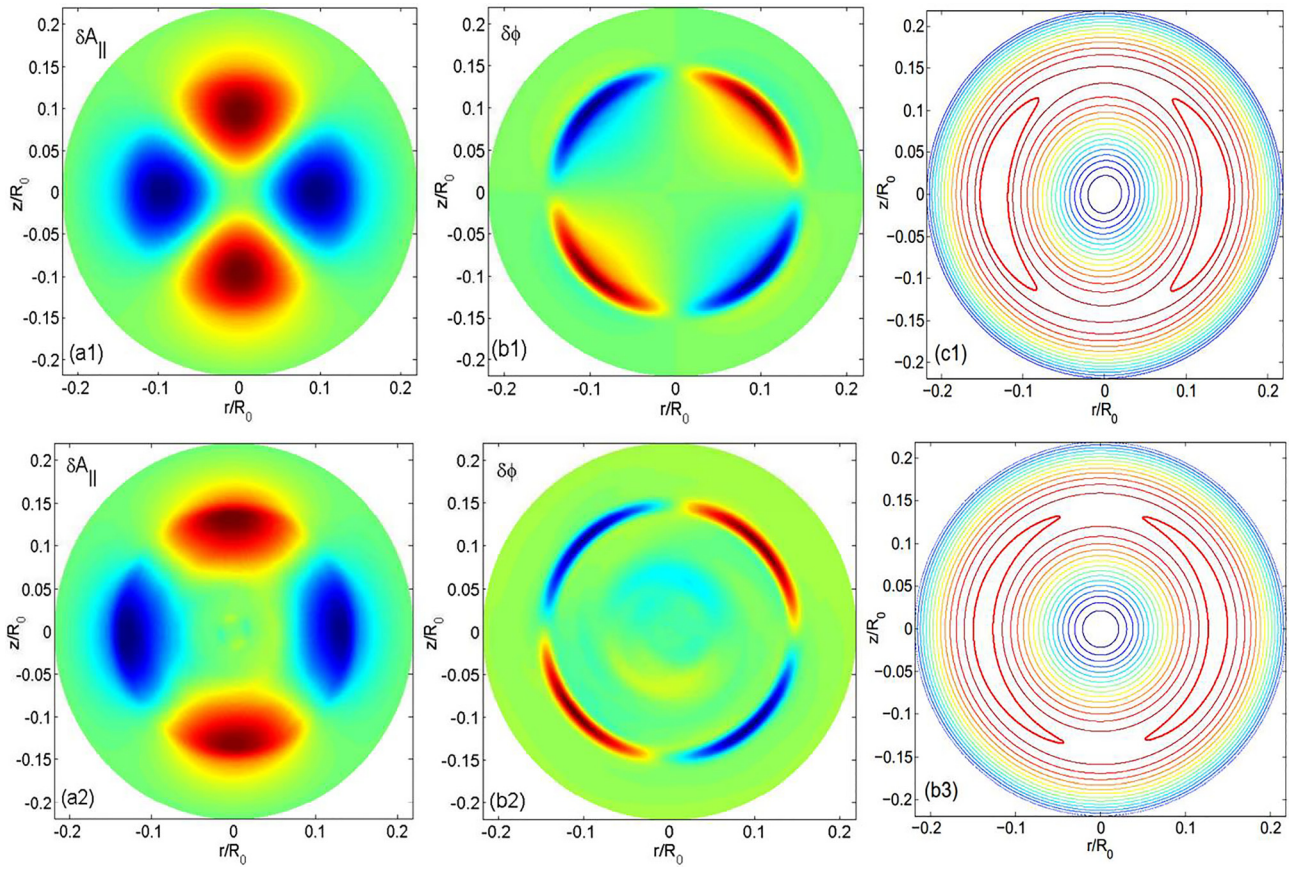


**FIG. 4.** The mode structure of (a) $\delta A_{||}$, (b) $\delta\phi$, and (c) the magnetic island, without the thermal kinetic effect of ions (top panel) or with the kinetic effect of thermal ions (bottom panel).

island of TMs (c) without kinetic thermal ions (top) and with kinetic thermal ions (bottom). Both the mode structure and magnetic island width shrink in the case with kinetic thermal ions given the same initial condition. Figure 4(c) shows a clear difference in the island width in these two cases. The island radial width of the TMs with kinetic ions is significantly smaller than that without kinetic ions at the same time, $t = 1.9 \times 10^{-5}$s. The growth rate decreases to $-0.12\omega_s$ when the ion kinetic effects are included, in comparison with $0.13\omega_s$ when the ions are unloaded. This indicates that the TM decays when the ion kinetic effect is considered. The phenomena are because the magnetic shear of the modified $q$ is still weak. The TMs could increase with a strong magnetic shear $q$, even when considering the kinetic effect of ions. There are two possible forms of the ion kinetic effects: one is through the finite Larmor radius (FLR) and finite orbit width effects, and the other is the wave-particle resonance with the ion acoustic waves (IAWs). In our calculations, it is found that the growth rate of the tearing mode is reduced by both the drift-kinetic and gyro-kinetic ions. The FLR effect is not important since the ion gyroradius is less than the magnetic island width scale (i.e., $\rho_i \ll w$), and the gyrocenter orbit width effect also plays a minor role because of $q\rho_i \ll w$ and $q\rho_i/\varepsilon \ll w$, where $\varepsilon = a/R_0$ is the inverse aspect ratio. On the other hand, we observed ion acoustic waves in the simulation. Therefore, the dominant kinetic effect is the wave-particle resonance with the IAW, which dissipates the energy from the driving force of TMs.

Moreover, with the kinetic ions added, we find that the island has a clockwise rotation, which is in the same direction of the ion diamagnetic drift direction. This rotation is more prominent when we calculate a case with $q = 1.75 + 4.66(\psi/\psi_w)^2$, where $\psi$ is the poloidal magnetic flux, $\psi_w$ is the poloidal magnetic flux of the plasma edge, and the $q = 2$ rational surface shifts to inner plasma. The measured frequency is 1.08 kHz, which is much smaller than the ion diamagnetic drift frequency.

Figure 4 shows that the radial mode width shrinks when kinetic thermal ions are added, and the net effect of kinetic ions on tearing modes is significant and stabilizing. We suspect that the kinetic ion interacts with the mode structure and damp the edge region of it, and this decaying finally leads to the decrease in the radial width of the magnetic island. To verify this argument, we further scan the temperature of thermal ions in order to study the kinetic effects of thermal ions. We also calculate the dependence of ion temperature on the island width and the growth rates of TMs. It is found that the island radial width increases with decreasing ion temperature. The growth rate for the three cases, $T_i = 0.01$, 0.1, and $1T_e$, are $0.10\omega_s$, $-0.09\omega_s$, $-0.12\omega_s$, respectively. It can be concluded that when the

ion temperature decreases, both the island radial width and the growth rates approach the values from fluid simulations. Therefore, this figure indeed confirms the ion thermal decaying effect.

### B. Nonlinear simulations of a model magnetic island in HL-2A

The current kinetic simulation cannot calculate the MHD timescale of the evolution of the tearing mode. One reason is due to the timescale, which we simulate is milliseconds, and the timescale in Ref. 24 is seconds, they differ by three orders of magnitude. The other reason is the lack of a saturation mechanism for tearing modes. Totally speaking, compared with the TM8 code, the amount of calculation of tearing modes will increase significantly, and the time step of each step will be limited by the Courant condition. Therefore, neither the GTC hybrid model nor the electron fluid model can simulate a long timescale. The entire MHD mode going from excitation to saturation cannot be simulated. However, even though the current kinetic simulation cannot calculate the MHD timescale of the evolution of the tearing mode, we can still study the nonlinear saturation of the model magnetic island by incorporating bootstrap current and by calculating the relationship between the growth rate of instability and the size of the initial magnetic island. Since the unstable NTM magnetic island can be obtained under the realistic equilibrium configuration of HL-2A, we calculate the linear evolution and nonlinear saturation of the model magnetic island using the true HL-2A configuration (i.e., q in green in Fig. 1, which is reconstructed from experimental data).

Figure 5 shows that the growth rate of the model magnetic island vs the initial magnetic island width at the ratio of perpendicular and parallel thermal diffusivity equals $10^8$. It can be seen from Fig. 5 that the magnetic islands in the linear phase will always grow. As the magnetic island grows, the instability enters the nonlinear growth phase. It can be seen from Fig. 5 that the model magnetic islands in the linear phase will always grow. As the magnetic island grows, the instability enters the nonlinear growth phase. In the simulation, when the model magnetic island is about $w/a = 20\%$, the model magnetic island grows fastest. As the magnetic island increases, the bootstrap current drive term decreases, resulting in a decrease in the growth rate of the model magnetic island, which eventually leads to nonlinear saturation (the saturation magnetic island width is about 34% in this case). The curve given in Fig. 5 is basically consistent with the modified Rutherford equation as shown in Ref. 24.

In addition, it should be noted that in order to suppress the effects of high-k perturbations in the simulation, we only reserve five toroidal and five poloidal modes, namely, n = 0, 1, 2, 3, and 4 and m = 0, 2, 4, 6, and 8. The retained modes depend on the results of our Fourier analysis. In the simulation, we perform the Fourier analysis of the key and physical quantities of different locations, such as dP. The results show that even if we enter the nonlinear phase, the low mode components of the basic physical quantities ($\delta A_{||}, \delta\phi, \delta n_e, \delta p$, etc.) always occupy a large amount of proportion for the low mode of m/n = 2/1 we studied. Taking the analysis of the poloidal mode shown in Fig. 6 as an example, Fig. 6(a) shows the poloidal distribution at the disturbance pressure at r = 0.39a, and Fig. 6(b) shows the poloidal Fourier analysis at that location. Our results show that the component of m = 0, 2, and 4 in the poloidal direction of the disturbance pressure occupies a very large increase proportion. Figure 6(c) shows the amplitude of magnetic perturbation for each

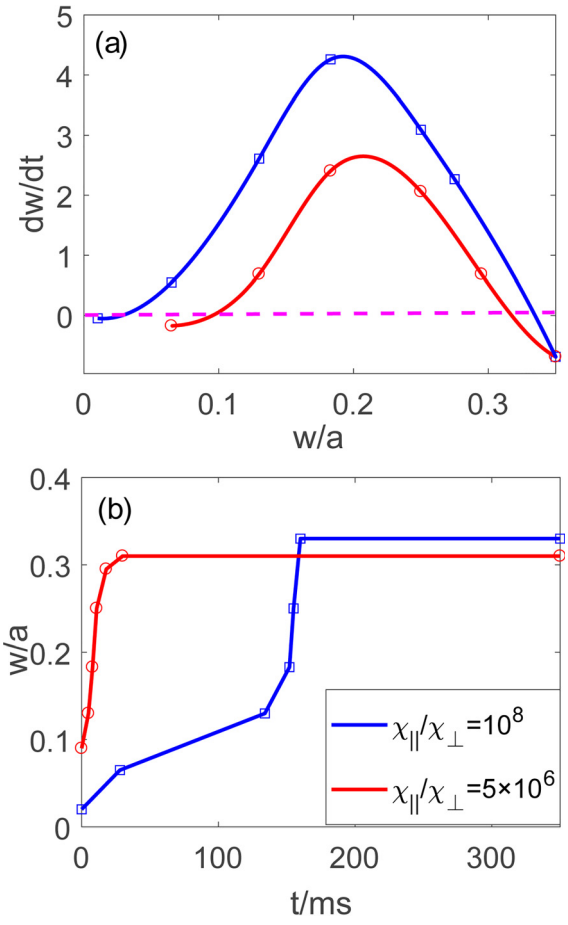


**FIG. 5.** (a) The growth rates of the model magnetic island vs the initial magnetic island width under different ratios of perpendicular and parallel thermal diffusivities. (b) The evolution of the magnetic island width corresponds to (a).

toroidal mode (n = 0, 1, 2, and 3) as a function of time. We could also see that only the m/n = 2/1 mode has a large increment. The m/n = 6/3 and higher mode components hardly have contributions to the mode growth. Therefore, the (2,1) mode amplitude here is dominant, and the pattern used here is credible when we only retain m = 0, 2, 4, 6, and 8 in the simulation.

### C. GTC nonlinear calculations of a model magnetic island in DIII-D

First, the equilibrium of DIII-D discharge 157402[57] reconstructed from the EFIT code[58] is used. This discharge has a prominent neoclassical tearing mode. However, this work is concentrated on the model magnetic island simulation and its suppression. Therefore, we ignore the effects of neoclassical bootstrap current [i.e., the bootstrap current terms in Eq. (9) were not incorporated] and consider only the 2D equilibrium profiles. The discharge parameters are given as follows: the major radius is $R_0 = 1.78$m, the minor radius is a = 0.58 m, the equilibrium plasma current is 790 kA, the $q = 2/1$ surface is $r = 0.54a$, and the toroidal magnetic field strength is $B_T = 2.06$T. In the

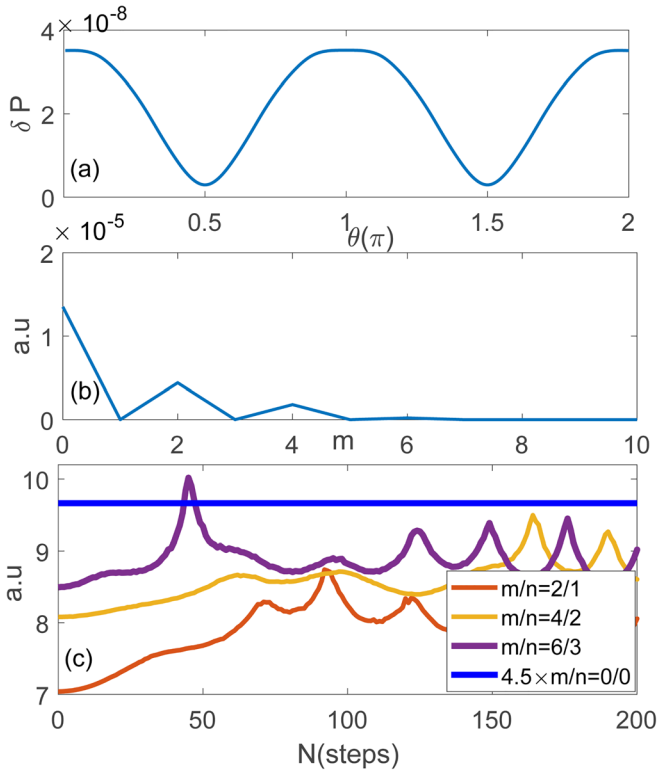


**FIG. 6.** (a) The Fourier analysis of the perturbation pressure in the poloidal direction at r = 0.39a. (b) The poloidal Fourier analysis at r = 0.39a. (c) The amplitude of magnetic perturbation for each toroidal mode (n = 0, 1, 2, 3,...) as a function of time.

simulations, we use the number of grids 128 × 512 × 32 in the radial, poloidal, and parallel directions, respectively. The configuration, equilibrium $q$ profile, electron density, and temperature profile are shown in Fig. 7. The resistivity is set to $\eta = 10^{-5}\,\Omega/\mathrm{m}$.

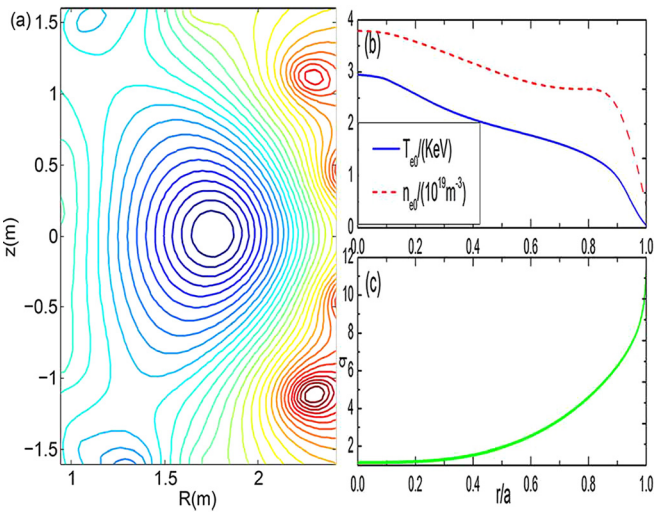


**FIG. 7.** (a) Poloidal magnetic structure of DIII-D equilibrium shot #157402, (b) radial profiles of electron density and temperature, and (c) safety factor.[57]

Figure 8 shows the mode structures of the parallel vector potential and electrostatic potential and the island structure at $t = 2.8 \times 10^{-5}$ s on the poloidal plane. The mode amplitude begins to increase linearly at this time, with the corresponding magnetic island width of about $0.127a$ at this time and the growth rate of $0.016\omega_s$. Figure 8 shows the (2, 1) magnetic island structures in the DIII-D configuration. Our simulations show that the model magnetic island is unstable in this DIII-D discharge, which may provide the seed island for the neoclassical tearing mode.

With equilibrium and plasma parameters given above, a 110 GHz electron cyclotron wave is launched with X-mode polarization from a port above the midplane, with the trajectories of the electron cyclotron wave shown in Fig. 9(a). With 1 MW ECW

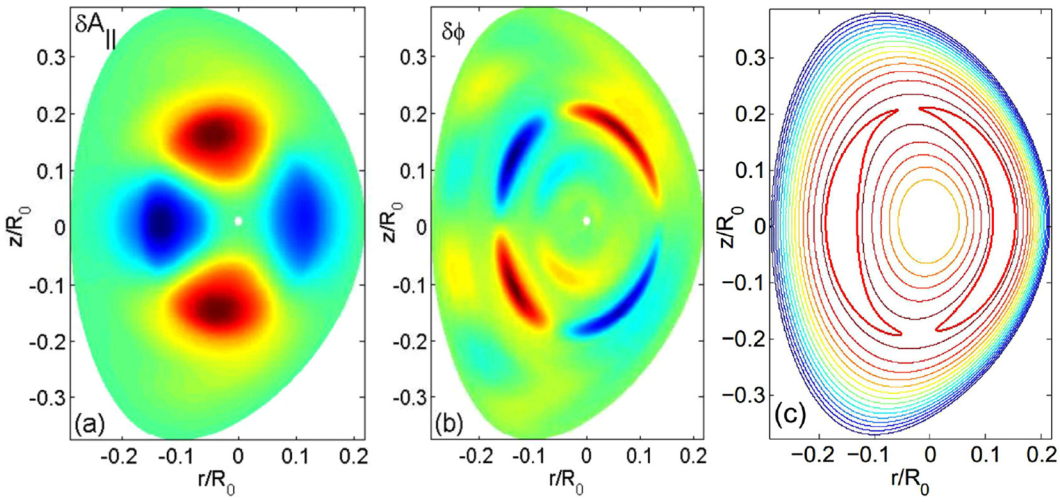


**FIG. 8.** Poloidal mode structures of (a) $\delta A_{||}$, (b) $\delta\phi$, and (c) the island structure at $t = 2.8 \times 10^{-5}$s.

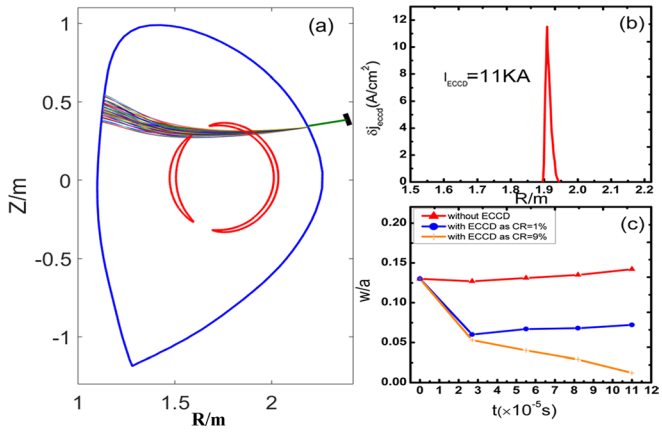


**FIG. 9.** (a) Electron cyclotron wave packet trajectories with the magnetic island, (b) ECCD current density vs normalized major radius, and (c) time evolution of the width w of the tearing mode magnetic island without ECCD and with different ECCD powers in the DIII-D tokamak.

power injected, the corresponding profile of driven current density with a poloidal angle of 100° and a toroidal angle of 193° is shown in Fig. 9(b). The absorption coefficient is 0.97, and the total driven current is 11 kA ($CR = 0.013$; the corresponding current density ratio, $\delta j_{eccd}/\delta j = 1.25$), with the radial deposition position located at $r/a = 0.5$ and a very narrow current drive profiles characteristic of ECCD, about 3.5 cm full width half maximum (FWHM), which is well suited for stabilizing the model magnetic island.

An example of the evolution of a model magnetic island width with and without the ECCD in Fig. 9(b) is shown in Fig. 9(c). Without ECCD, the model magnetic island grows slowly. The red curve in Fig. 7(c) still represents the growth phase of the model magnetic island, where the magnetic island width can be approximately fitted in an exponential form of $0.12 \times \mathrm{Exp}(0.014t)$. The stability is improved with ECCD since the magnetic island width decreases with ECCD. However, the island width does not decrease to zero in this case. The ECCD only reduces the growth of the model magnetic island, rather than fully stabilizing it. This is due to the low ECCD current (11 kA), significantly below the equilibrium current (790 kA), and that a higher

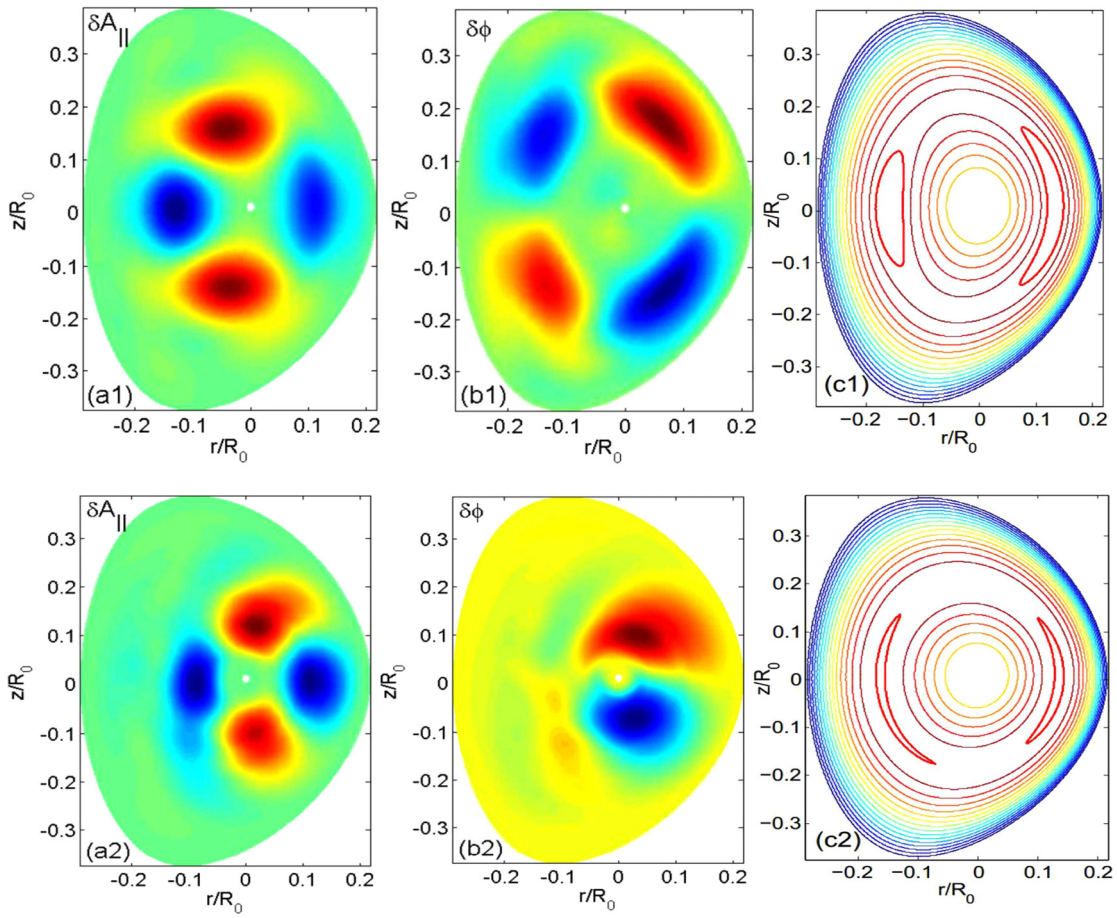


**FIG. 10.** Poloidal mode structure of $\delta A_{||}$ (left column), $\delta\phi$ (middle column), and the island map (right column) without (top panel) and with kinetic thermal ions (bottom panel) in DIII-D.

input ECW power is required to entirely suppress the model magnetic island. Indeed, if the value of CR is increased in the simulation, the model magnetic island is almost suppressed when CR equals 0.09 [as depicted by the orange line in Fig. 9(c)]. The island size decreases to a very small width, and the corresponding decay rate is $0.08\omega_s$.

It should be noted that due to numerical constraints, it is currently difficult for the GTC to simulate dynamically the entire time evolution of the magnetic islands, from the linear growth of a small island to nonlinear saturation of the large island. Instead, the approach we take in this work is to perform GTC nonlinear simulations of the island stability for various initial island sizes. We find that when the initial island size is small, the island size increases in time, and we can measure the growth rate. The growth rate is smaller when the initial island size is larger. When the initial island size is large enough, the growth rate is zero, and we call this island size as the saturated island width. If the initial island size is larger than the saturated island width, we find that the island decays in GTC simulation.

We carry out the GTC kinetic simulations by loading 20 ions in every cell in the DIII-D configuration. Figure 10 shows the mode structure [(a) and (b)] and the island map (c) without kinetic thermal ions (top) and with kinetic thermal ions (bottom). In both cases, we do not consider the effect of ECCD and assume that the ion and electron temperature profiles are the same, namely, $T_i = T_e$. The radial width of the model magnetic island with kinetic thermal ions is significantly smaller than that without kinetic thermal ions. When considering the ion kinetic effects, the growth rate decreases to $0.009\omega_s$, compared with the growth rate of the model magnetic island without kinetic ions, $0.016\omega_s$.

We conclude that kinetic effects of thermal ions can reduce the growth rate of the model magnetic island in a tokamak plasma. This result is consistent with analytical calculations,[31,59] which show that the kinetic contribution tends to reduce $\Delta'$ for the toroidal equilibria, and can lead to the stability for the magnetic island.

## IV. CONCLUSIONS

In summary, we have investigated the influence of the electron cyclotron current drive on the m/n = 2/1 magnetic island using gyrokinetic simulations in HL-2A and DIII-D configurations. The model magnetic island evolution is calculated with a massless electron fluid model, and the ECCD current source is obtained by ray-tracing and the Fokker–Planck method. We find that the stability of the tearing mode depends on the magnetic shear. The TM magnetic island is found to be perfectly stabilized by a continuous 1 MW 68 GHz X2-mode in the HL-2A tokamak since the linear growth of TMs becomes negative when we turn on the ECCD. Our simulation also finds that a helicoidal current drive is more efficient than a continuous ECCD. In the DIII-D tokamak, the (2,1) magnetic island is unstable with the real experimental data as the simulation input. The model magnetic island is only partially stabilized with the 1 MW 110 GHz X2-mode due to the low current ratio, namely, due to the inadequate power input. At this time, to completely suppress the model magnetic island, it is necessary to use a larger wave power (CR = 0.09) or a modulated ECCD.

The ion kinetic effect on the tearing mode magnetic island stabilization is demonstrated. We calculated the evolution of TMs on the HL-2A device considering the thermal ion. When loading the thermal ion, the linear growth rate of TMs will decrease, the mode structure will be narrowed, and there will be a rotation in the ion diamagnetic direction. The frequency, measured in the simulation, is 1.08 kHz, which is much lower than the diamagnetic drift frequency of the ion. Although the results we obtained are similar to those obtained by Cai *et al.*,[31] since we consider thermal ions and they consider high-energy ions, the comparison between the two is put into the next step, that is, to study the effect of energetic particles on TMs. For the effects of thermal ions, the simulations on the HL-2A device are similar to those on the DIII-D device, i.e., thermal ions also cause a decrease in the growth rate of the magnetic island. When ion temperature increases, the typical (2,1) mode structure will no longer appear so that significant mode structure rotation cannot be observed.

Our simulations in a certain machine configuration will contribute to the design of the real-time control system of the TMs and provide useful suggestions to TMs or neoclassical tearing mode control experiments for fusion devices, especially for HL-2A and DIII-D tokamaks. Meanwhile, the calculation is part of a longer term plan of building a first-principles model and a self-consistent simulation of the neoclassical tearing mode in fusion plasmas.

## ACKNOWLEDGMENTS

The authors would like to thank W. W. Heidbrink at UCI for providing the EFIT equilibrium of DIII-D shot 157402 and Min Xu, L. W. Yan, and Jun Wang at SWIP; Lei Shi and Jian Bao at UCI; and Youjun Hu at ASIPP for fruitful discussions. J. C. Li would like to thank S. Y. Liang at SWIP for providing the experimental data in HL-2A. This work was supported by the ITER-China program (Nos. 2018YFE0303102, 2017YFE0301702, and 2014GB107004), the NSFC (Nos. 11905109 and 11947238), U.S. DOE SciDAC ISEP, and the China Postdoctoral Science Foundation (No. 2018M640230).

## REFERENCES

[1]G. Giruzzi, M. Zabiego, T. A. Gianakon, X. Garbet, A. Cardinali, and S. Bernabei, Nucl. Fusion **39**, 107 (1999).
[2]J. Walker, Phys. Rev. E **98**, 033209 (2018).
[3]] R. J. La Haye, Phys. Plasmas **13**, 055501 (2006).
[4]E. Kim, Phys. Rev. E **76**, 025401 (2007).
[5]R. J. La Haye, R. Prater, R. J. Buttery, N. Hayashi, A. Isayama, M. E. Maraschek, L. Urso, and H. Zohm, Nucl. Fusion **46**, 451 (2006).
[6]Y. R. Lin-Liu, V. S. Chan, and R. Prater, Phys. Plasmas **10**, 4064 (2003).
[7]R. I. Pinsker, Phys. Plasmas **8**, 1219 (2001).
[8]R. Fitzpatrick, Nucl. Fusion **33**, 1049 (1993).
[9]Q. Hu, Q. Yu, B. Rao, Y. H. Ding, X. W. Hu, and G. Zhuang, and J-TEXT Team, Nucl. Fusion **52**, 083011 (2012).
[10]M. Garcia-Munoz, H.-U. Fahrbach, S. D. Pinches, V. Bobkov, M. Brudgam, M. Gobbin, S. Gunter, V. Igochine, Ph. Lauber, M. J. Mantsinen, M. Maraschek, L. Marrelli, P. Martin, P. Piovesan, E. Poli, K. Sassenberg, G. Tardini, H. Zohm, and ASDEX Upgrade Team, Nucl. Fusion **49**, 085014 (2009).
[11]G. Gantenbein, H. Zohm, G. Giruzzi, S. Günter, F. Leuterer, M. Maraschek, J. Meskat, Q. Yu, ASDEX Upgrade Team, and ECRH-Group, Phys. Rev. Lett. **85**, 1242 (2000).
[12]C. C. Petty, R. J. La Haye, T. C. Luce, D. A. Humphreys, A. W. Hyatt, J. Lohr, R. Prater, E. J. Strait, and M. R. Wade, Nucl. Fusion **44**, 243 (2004).
[13]A. Isayama, Y. Kamada, T. Ozeki, S. Ide, T. Fujita, T. Oikawa, T. Suzuki, Y. Neyatani, N. Isei, K. Hamamatsu, Y. Ikeda, K. Takahashi, K. Kajiwara, and JT-60 Team, Nucl. Fusion **41**, 761 (2001).
[14]Z. Chang, J. D. Callen, E. D. Fredrickson, R. V. Budny, C. C. Hegna, K. M. McGuire, M. C. Zarnstorff, and TFTR Group, Phys. Rev. Lett. **74**, 4663 (1995).
[15]R. J. La Haye, P. A. Politzer, and D. P. Brennan, Nucl. Fusion **48**, 015005 (2008).

[16]X. R. Duan, Y. Liu, M. Xu, L. W. Yan, Y. Xu, X. M. Song, J. Q. Dong, X. T. Ding, L. Y. Chen, B. Lu, D. Q. Liu *et al.*, Nucl. Fusion **57**, 102013 (2017).
[17]Y. Liu, Phys. Rev. E **84**, 016403 (2011).
[18]M. Kong, T. C. Blanken, F. Felici, C. Galperti, E. Maljaars, O. Sauter, T. Vu, F. Carpanese, A. Merle, J.-M. Moret, F. Pesamosca, E. Poli, M. Reich, A. A. Teplukhina, TCV Team, and EUROfusion MST1 Team, Nucl. Fusion **59**, 076035 (2019).
[19]B. A. Hennen, E. Westerhof, P. W. J. M. Nuij, J. W. Oosterbeek, M. R. de Baar, W. A. Bongers, A. Bürger, D. J. Thoen, M. Steinbuch, and TEXTOR Team, Plasma Phys. Controlled Fusion **52**, 104006 (2010).
[20]G. Gantenbein, A. Keller, F. Leuterer, M. Maraschek, W. Suttrop, H. Zohm, and ASDEX Upgrade Team, "Investigations on m = 2, n = 1 tearing mode stabilisation with ECRH at ASDEX Upgrade," in *Proceedings of the 30th EPS Conference on Controlled Fusion and Plasma Physics, St. Petersburg, Russia, 2003*, edited by R. Koch and S. Lebedev (European Physical Society, Geneva, 2003), Vol. 27A, p. P-1.187 (CD-ROM).
[21]R. J. La Haye, S. Günter, D. A. Humphreys, J. Lohr, T. C. Luce, M. E. Maraschek, C. C. Petty, R. Prater, J. T. Scoville, and E. J. Strait, Phys. Plasmas **9**, 2051 (2002).
[22]R. Prater, R. LaHaye, T. C. Luce, C. C. Petty, E. J. Strait, J. R. Ferron, D. A. Humphreys, A. Isayama, J. Lohr, K. Nagasaki, P. A. Politzer, M. R. Wade, and A. S. Welander, Nucl. Fusion **47**, 371 (2007).
[23]Q. Yu, X. D. Zhang, and S. Gnter, Phys. Plasmas **11**, 1960 (2004).
[24]J. Li, X. Ji, J. Dong, Y. Hu, S. Liu, L. Yan, and HL-2A Contributors, Phys. Plasmas **26**, 032505 (2019).
[25]T. G. Jenkins and E. D. Held, J. Comput. Phys. **297**, 427 (2015).
[26]S. Wang, Z. W. Ma, and W. Zhang, Phys. Plasmas **23**, 052503 (2016).
[27]J. Pratt, G. T. Huijsmans, and E. Westerhof, Phys. Plasmas **23**, 102507 (2016).
[28]O. Fvrier, P. Maget, H. Lutjens, and P. Beyer, Plasma Phys. Controlled Fusion **59**, 044002 (2017).
[29]A. M. Popov, R. J. La Haye, Y. Q. Liu, M. Murakami, N. N. Popova, and A. D. Turnbull, Phys. Plasmas **9**, 4229 (2002).
[30]T. G. Jenkins, S. E. Kruger, C. C. Hegna, D. D. Schnack, and C. R. Sovinec, Phys. Plasmas **17**, 012502 (2010).
[31]H. Cai, S. Wang, Y. Xu, J. Cao, and D. Li, Phys. Rev. Lett. **106**, 075002 (2011).
[32]H. Cai and G. Fu, Phys. Plasmas **19**, 072506 (2012).
[33]W. A. Hornsby, P. Migliano, R. Buchholz, S. Grosshauser, A. Weikl, D. Zarzoso, F. J. Casson, E. Poli, and A. G. Peeters, Plasma Phys. Controlled Fusion **58**, 014028 (2016).
[34]Z. Lin, T. S. Hahm, W. W. Lee, W. M. Tang, and R. B. White, Science **281**, 1835 (1998).
[35]Z. Lin, W. M. Tang, and W. W. Lee, Phys. Rev. Lett. **78**, 456 (1997).
[36]W. Zhang, Z. Lin, and L. Chen, Phys. Rev. Lett. **101**, 095001 (2008).
[37]H. S. Zhang, Z. Lin, and I. Holod, Phys. Rev. Lett. **109**, 025001 (2012).
[38]Z. Wang, Z. Lin, I. Holod, W. W. Heidbrink, and B. Tobias, Phys. Rev. Lett. **111**, 145003 (2013).
[39]Z. Lin, I. Holod, L. Chen, P. H. Diamond, T. S. Hahm, and S. Ethier, Phys. Rev. Lett. **99**, 265003 (2007).
[40]J. McClenaghan, Z. Lin, I. Holod, and W. Deng, Phys. Plasmas **21**, 122519 (2014).
[41]D. J. Liu, W. L. Zhang, J. McClenaghan, J. Q. Wang, and Z. Lin, Phys. Plasmas **21**, 122520 (2014).
[42]J. C. Li, C. J. Xiao, Z. H. Lin, and K. J. Wang, Phys. Plasmas **24**, 082508 (2017).
[43]X. Q. Xue, Phys. Rev. E **78**, 016406 (2008).
[44]R. W. Harvey, Bull. Am. Phys. Soc. **39**, 1626 (1994).
[45]O. Fevrier, P. Maget, H. Lütjens, J. F. Luciani, J. Decker, G. Giruzzi, M. Reich, P. Beyer, E. Lazzaro, and S. Nowak, Plasma Phys. Controlled Fusion **58**, 045015 (2016).
[46]I. Holod, W. L. Zhang, Y. Xiao, and Z. Lin, Phys. Plasmas **16**, 122307 (2009).
[47]J. Bao, D. Liu, and Z. Lin, Phys. Plasmas **24**, 102516 (2017).
[48]W. W. Lee, J. Comput. Phys. **72**, 243 (1987).
[49]A. Brizard and T. Hahm, Rev. Mod. Phys. **79**, 421 (2007).
[50]A. M. Dimits and W. W. Lee, J. Comput. Phys. **107**, 309 (1993).
[51]S. E. Parker and W. W. Lee, Phys. Fluids B **5**, 77 (1993).
[52]W. Deng, Z. Lin, and I. Holod, Nucl. Fusion **52**, 023005 (2012).
[53]W. Zhang, S. Wang, and Z. W. Ma, Phys. Plasmas **24**, 062510 (2017).
[54]M. Maraschek, G. Gantenbein, Q. Yu, H. Zohm, S. Günter, F. Leuterer, A. Manini, ASDEX Upgrade Team, and ECHR Group, Phys. Rev. Lett. **98**, 025005 (2007).
[55]J. Wang, C. Xiao, X. Wang, X. Ji, and Y. Liu, Plasma Phys. Controlled Fusion **54**, 122001 (2012).
[56]J. C. Li, X. Y. Gong, J. Q. Dong, P. W. Zheng, S. D. Song, Q. D. Gao, and D. Du, Phys. Plasmas **22**, 062512 (2015).
[57]W. W. Heidbrink, M. E. Austin, C. S. Collins, T. Gray, B. A. Grierson, G. J. Kramer, M. Lanctot, D. C. Pace, M. A. Van Zeeland, and A. G. Mclean, Nucl. Fusion **55**, 083023 (2015).
[58]L. L. Lao, H. S. John, R. D. Stambaugh, A. G. Kellman, and W. Pfeiffer, Nucl. Fusion **25**, 1611 (1985).
[59]Y. Liu, R. J. Hastie, and T. C. Hender, Phys. Plasmas **19**, 092510 (2012).